# THE FABRICATION AND CHARACTERIZATION OF A LABEL-FREE GRAPHENE FIELD EFFECT TRANSISTOR BIOSENSOR

Peter M. Wojcik

Department of Physics
Oregon State University
Corvallis, OR

August 2012

# ABSTRACT

This project addresses the fabrication and characterization of a graphene field effect transistor (GFET) for use as a biological sensing device. The graphene used in these experiments was grown via chemical vapor deposition (CVD). The CVD method is a cost and time effective technique to produce graphene, and can satisfy the needs for the commercialization of a portable biological sensing device. We demonstrate a fabrication method for developing a label-free aptamer modified CVD graphene-based field effect transistor (FET) biosensor. These devices were used to detect thrombin protein using a microfluidic mass flow system. The thrombin biological sensing experiment showed a measurable change in resistance in our device when thrombin protein was added to the system. The resistance increased after the addition of a buffer solution suggesting that thrombin protein was bound to the aptamer modified graphene surface, and was removed by the buffer solution. This experiment suggests that a label-free aptamer modified CVD graphene-based FET biosensing device can be used for accurate protein detection.

# PREFACE

This paper was submitted to the Department of Physics at Oregon State University on August 16, 2012 in partial fulfillment of the requirements for the degree of Master of Science in Physics. All work presented in this paper, including figures, is original and should not be copied or reproduced without permission.

When I joined Ethan Minot's group in January 2012, Ethan initially gave me the task of fabricating a graphene field effect transistor. After a prototype device was made, I wanted to reproduce similar results from a paper which used an aptamer modified graphene field effect transistor (GFET) to detect a specific protein without the use of labels. I began with the development of a new set of devices which incorporated improved fabrication techniques. These devices were a drastic improvement to the prototypes and showed us that an aptamer modified GFET biosensing device may be possible. Grant Saltzgaber joined the project during the fabrication of the new set of devices and developed a functionalization scheme for the thrombin aptamer. We eventually found success in detecting thrombin protein using our devices.

The success of this project has been attributed to many people. I would like to thank Dr. Ethan Minot for giving me the opportunity to work in his group. His support and guidance made the scope of this project practical for the amount of time I had left at Oregon State University. Thank you to Tal Sharf, Tristan DeBorde, and Dr. Landon Prisbrey for their generous and helpful support. Your patience and knowledge is inspiring and has been invaluable for the success of this project. Thank you Grant Saltzgaber for deciding to become a part of this project. This could not have been done without your assistance and support.

Many people contributed to the work in this paper. Tal Sharf took electrical measurements of the preliminary devices. Grant Saltzgaber took electrical measurements of the biosensing devices and performed the thrombin aptamer functionalization scheme. Former Minot group member, Dr. Matthew Leyden, who

now works for Nanotechnology Biomachines, Inc. grew and supplied the graphene for the biosensing devices. Jenna Wardini assisted with the growth of the graphene used in the preliminary devices. Josh Kevek gave support with the growth of graphene used in the preliminary devices, the graphene transfer process, as well as the device fabrication process.

*Peter M. Wojcik*
*August 16, 2012*
*Corvallis, OR*

TABLE OF CONTENTS

# LIST OF FIGURES

CHAPTER 1

# Introduction

## 1.1 Graphene

Graphene is a two-dimensional mono layer of carbon atoms. Six electrons surround the nucleus in the carbon atom and are arranged in the electron configuration $1s^2$ $2s^2$ $2p^2$. In graphene the outer 2s, $2p_x$ and $2p_y$ orbitals combine or hybridize to form $sp^2$ hybrid orbitals. The $sp^2$ hybrids form three planar orbitals. These planar orbitals form sigma bonds between adjacent carbon atoms oriented at an angle of 120° with respect to each other and are responsible for the hexagonal structure of a graphene lattice. The $p_z$ orbital lies perpendicular to the three sp2 orbitals and contains the remaining electron which is responsible for the unique electronic characteristics of graphene.[1]

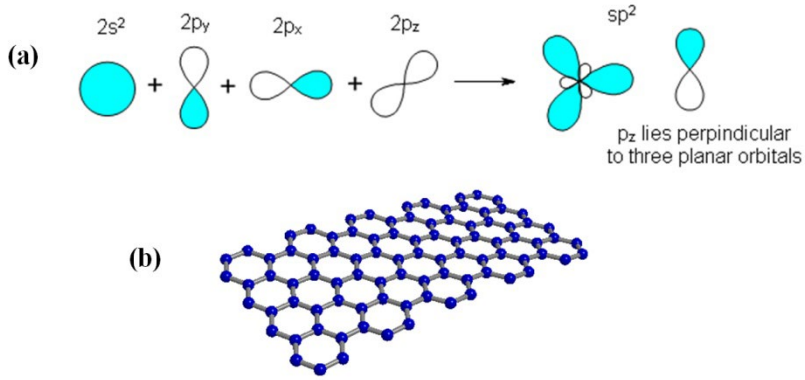


**Figure 1.1 (a)** Hybridization of a $sp^2$ orbital and **(b)** graphene lattice.

Recently, the desire for the large scale production of high quality defect free graphene has increased in the scientific community because of graphene's scalability, high carrier mobility and chemical stability at room temperature in air.[2] Carbon is also one of the most abundant elements on earth which makes graphene cost effective and plentiful.

In 2004, a group at the University of Manchester was able to produce single layer graphene using a technique called mechanical exfoliation which entails the repeated pealing of pyrolytic graphite.[3] Mechanical exfoliation is a reliable method for producing high quality defect free graphene, however it can only cover very small areas[3] and is therefore not suitable for the large scale production of graphene. There

are several other methods for producing graphene.[4] A process that is cost and time effective and also able to produce large scale defect free graphene is desired to take advantage of carbon's abundance and graphene's unique electrical properties.

Chemical vapor deposition (CVD) is a cost and time effective method for producing high quality graphene in large quantities. A typical CVD process for graphene is performed under vacuum and uses heat to break apart the atoms in a gaseous hydrocarbon such as methane. The remaining carbon atoms then align themselves atop a high purity copper film in the distinctive hexagonal structure of graphene (Fig 1.2). The graphene film can then be transferred to the desired substrate through various techniques.

A disadvantage of the CVD process is that the growth and transfer process which can produce defects in the graphene lattice. Perfecting the CVD process is an ongoing goal and is necessary for the commercialization of the many useful applications of graphene.

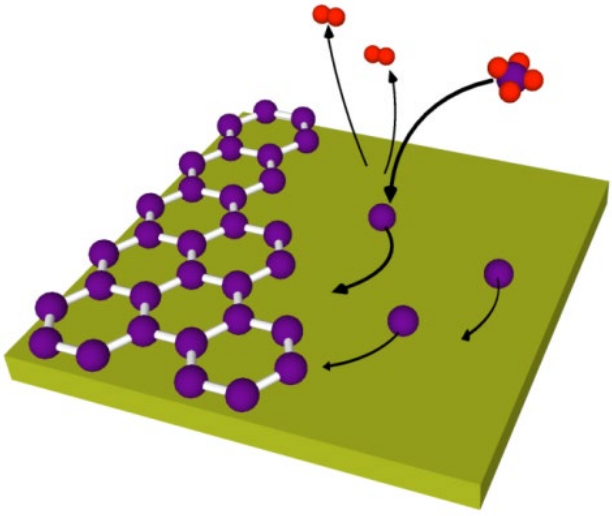

**Figure 1.2** Drawing of the CVD process. The orange substrate is copper foil.

Graphene transistors are a promising candidate to replace traditional silicon semiconductor devices in integrated circuits[5] due to their high carrier mobility[3] and ability to maintain performance low temperatures.[6] Graphene exhibits a high optical

transmittance which makes it a possible alternative to conventional transparent conductive electrodes such as indium tin oxide.[7] Graphene's extraordinary electrical properties are also presenting new prospects as electrical based chemical and biological sensors.[8]

## 1.2 Biosensors

A biosensor is a device that is capable of detecting specific biological molecules. A blood glucose monitor is an example of a commercially available biosensor. It is an accurate and invaluable tool for diabetics who need to monitor their glucose levels. Other types of biological sensors are used to detect protein,[9] antibodies,[10] and DNA.[11] The motivation to create accurate biosensing devices is fueled by their valuable applications in gene analysis,[11] detection of biological warfare agents,[11] and the detection of potentially life threatening diseases like prostate cancer.[12] In gene analysis, the detection of genetic mutations can allow medical professionals to identify diseases even before any symptoms appear.[11]

Biosensors can be simplified into two categories, label and non-label based. Label based technologies chemically modify a biological molecule with a fluorescent tag that can be seen with a fluorescent microscope, however this method requires a lengthy labeling process and expensive detection equipment.[13] Label-free technologies do not require any tagging to identify specific molecules and are ideal for quick and accurate diagnosis. Surface Plasmon resonance,[14] carbon nanotube (CNT),[15] graphene,[10] and silicon nanowire[16] biological sensors are examples of label-free technologies that are currently under development.

The early detection of certain diseases such as prostate cancer is imperative to increase a patient's likely hood of survival. Label-free technologies are able to satisfy the need for a timely method of biological detection by providing real-time, accurate, specific detection of biological diseases.[10,15,17]

### *1.2.1 Graphene Biosensors*

A point-of-care (POC) biological sensor is a technology that has recently received a lot of attention because of their ability to process several biological markers simultaneously.[18] POC systems will also allow technology and information to be available to a much wider population, which in the past has only been accessible to leading cancer centers.[18] Biosensors which incorporate nanomaterials such as CNTs, nanowires and graphene are able to satisfy the needs of a highly accurate and portable POC biological sensor. Graphene is of particular interest for use in POC biosensors because of its nanoscale dimensions, large surface area, and high carrier mobility.

There are many graphene biosensing technologies currently being investigated. A group at Fuzhou University has shown that graphene oxide (GO) is a potential platform for the selective detection of DNA and proteins, and compared to CNTs, GO's low cost and large production scales make it a promising candidate for biosensing devices.[19] Recently, a graphene based fluorescence resonance energy transfer (FRET) sensor was developed and reported to have detected thrombin to limits as low as 31.3 pM, which is two orders of magnitude lower than CNT based fluorescence sensors.[9] Other biosensing technologies incorporate graphene into a field effect transistor for use as a biological sensing device.[10,20,21]

### *1.2.2 Graphene Field Effect Transistor Biosensors*

A field effect transistor (FET) is a voltage-controlled device which is capable of varying a current across a semiconducting channel by the application of an electric field. In a graphene field effect transistor (GFET) the graphene sheet acts as the semiconducting channel between two metal source and drain electrodes which lie atop an electrical insulator such as $SiO_2$. When charged biological molecules bind on the surface of the semiconducting graphene sheet in the GFET there is a measurable change in resistance. The GFET device is able to act as a real-time all electronic biosensor based on this detection principle.

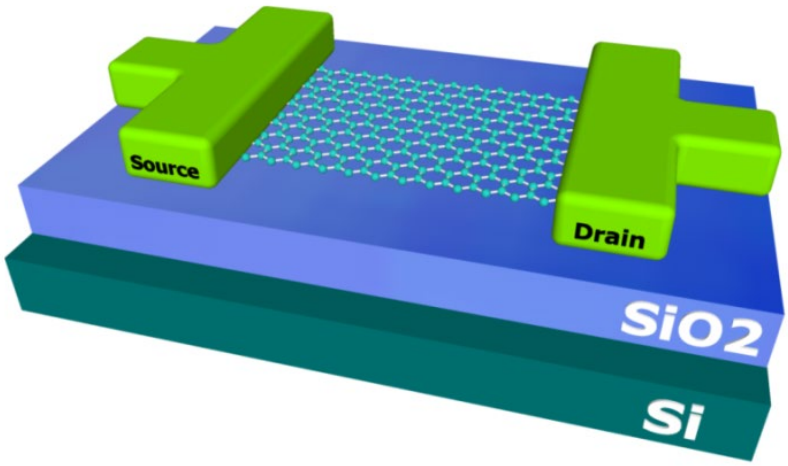


**Figure 1.3** A graphene field effect transistor.

Ohno et al. successfully used a label-free GFET device to detect bovine serum albumin [21], Immunoglobulin E,[10] and show that GFET's have sensitivity under several hundred picomoles per liter.[22] This recent work has shown that GFET biosensing devices are promising candidates over CNT devices, however the graphene used in these experiments was obtained through mechanical exfoliation. As discussed previously, this method is not practical for cost and time effective production of a GFET biosensing device.

The need for a cost effective POC graphene based biological sensor will require the use of a GFET device which uses CVD graphene. Several groups are currently experimenting with label-free GFETs which incorporate CVD graphene,[6,23,24] and have successfully detected DNA hybridization,[24] glucose oxidase,[23] and glutamic dehydrogenase.[23] The detection limits of the glucose and glutamate sensors are comparable to CNT,[25] and graphene based electrochemical biosensors which use methods to obtain graphene other than mechanical exfoliation,[26] however are still inferior to nanowire,[27] and CNT[28] based electrochemical biosensors. The recent attention and work dedicated to the large scale production of high quality graphene will likely show that graphene is a practical and superior alternative to other nanomaterials which are incorporated into biosensors.

## 1.3 Thrombin Protein

Thrombin protein is produced by the body and has an important role in the blood clotting or coagulation process,[29] and the regulation of tumor growth.[30] The selective and sensitive detection of thrombin may be useful in surgical procedures and cardiovascular disease therapy.[29] There have been many efforts to produce a sensitive biological sensor for the detection of thrombin.[9,31] In the past, thrombin has been optically detected using a fluorescence based tag,[31] which we have previously discussed as a slow and costly method for detection. In this paper we will address the feasibility of a CVD graphene-based label-free FET biosensor to accurately detect thrombin.

CHAPTER 2

# Graphene Characterization Theory

## 2.1 Electrical Characterization

### *2.1.1 Drude Model for Metals*

Three years after the discovery of the electron by J.J. Thomsen in 1897, P. Drude constructed a theory of electrical and thermal conduction which applied the kinetic theory of gases to metals.[32] The kinetic theory applied to metals assumes that electrons behave classically, i.e., they can be treated like solid spheres which travel in straight line paths until they collide with each other or imperfections in the solid. Drude's model can used to describe and quantify some of graphene's unique electrical characteristics.

Ohm's Law, which can be explained using Drude's model, states that the potential $V$across a conducting wire is proportional to the current $I$ flowing through the wire, or

$$V = IR \tag{2.1}$$

where $R$ is the resistance of the conducting wire, and is measured in Ohms or equivalently Volts/Ampere. The resistance is independent of the magnitude of the current or potential drop but depends on the wire's dimensions.

If we assume that the current $I$ is distributed evenly over the cross sectional area $A$ of our conducting wire, then the current density is $J = I/A$. If there exists an electrical field **E**, it will exert forces on the moving charges and hence there should be some functional relationship between **E** and **J**. This relationship can be expressed as

$$\mathbf{E} = \rho\mathbf{J} \tag{2.2}$$

where $\rho$ is a proportionality constant called the resistivity. This constant eliminates the dependence on the dimensions of the wire and is a measure of how well a conductor is able to oppose the flow of an electrical current. Equation (2.2) is typically expressed in terms of the inverse of the resistivity, or the conductivity $\sigma$ as

$$\mathbf{J} = \sigma \mathbf{E} \tag{2.3}$$

This relationship is the macroscopic equivalent to Ohm's law for a linear isotropic homogeneous conductor and is often referred to as the microscopic form of Ohm's law.[33]

If we again consider the case where there exists an electrical field **E**, there will be a mean velocity directed opposite to the applied field. This average velocity is called the drift velocity and is related to the electric field by

$$\mathbf{v}_d = -\mu_e \mathbf{E} \tag{2.4}$$

where $\mu_e$ is called the electron mobility and tells us how fast electrons can travel through a conductor when an applied electric field **E** exerts a force on them.

Let us consider $n$ number of electrons per unit volume all traveling at velocity $\mathbf{v}_d$ through a cross sectional area $A$. The electrons will move a distance $v\,dt$ in time $dt$ and $nvAdt$ electrons will pass through the cross sectional area $A$. The charge passing through $A$ in time $dt$ will be $-nevAdt$ and the current density is

$$\mathbf{J} = -ne\mathbf{v}_d \tag{2.5}$$

Using equations (2.3), (2.4), and (2.5) we can now relate the conductivity to mobility by

$$\sigma = ne\mu_e \tag{2.6}$$

### *2.1.2 Drude Model for a Semiconducting Sheet*

Note that the equation for conductance is only valid when the conductivity is only due to electrons. In a p-type semiconductor the conductivity is due to holes, in which case the conductance is given by

$$\sigma = pe\mu_h \tag{2.7}$$

where $p$ is the hole density and $\mu_h$ is the hole mobility. In a semiconductor which conducts by electrons and holes the conductivity is

$$\sigma = e(n\mu_e + p\mu_h) \tag{2.8}$$

Another useful quantity for describing the electrical properties of graphene is sheet resistance, which is a measure of resistance of very thin films which are uniform in thickness. Let's consider a current $I$ flowing uniformly through a wire conductor of length $L$. The potential across that length will be $V = EL$, and from eq. (2.2) gives $V = \rho IL/A$. Therefore, the resistance and resistivity are related by

$$R = \rho\frac{L}{A} \tag{2.9}$$

If we now consider the cross sectional area $A$ to have some width $W$ and thickness $t$ then (2.9) becomes

$$R = \rho\frac{L}{Wt} = \frac{\rho}{t}\frac{L}{W} = R_s\frac{L}{W} \tag{2.10}$$

where $R_s = \rho/t$ and is called the sheet resistance.

### *2.1.3 Band Structure of Graphene*

Free electron theory is an accurate model to predict the electrical characteristics of graphene and other materials however it fails at describing the differences between metals, semimetals, semiconductors, and insulators.

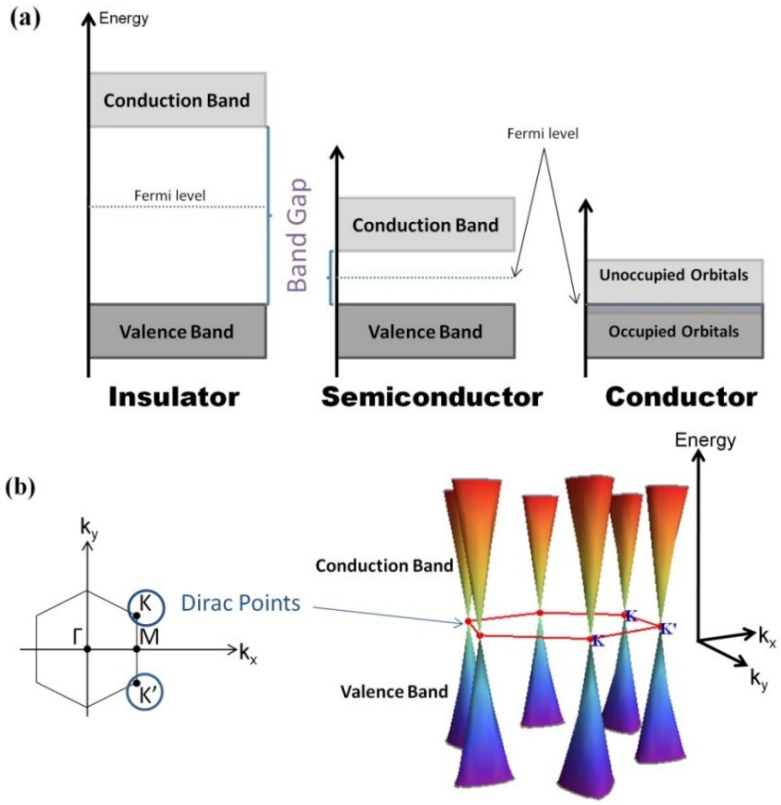


**Figure 2.1** Energy Diagrams. **(a)** Insulator, semiconductor, and conductor energy bands. **(b)** First Brillouin zone of a graphene lattice (left) and 3-dimensional representation of graphene's conical energy bands plotted as a function of wavevector **k** (right). The Dirac points are located at the six K points in graphene's unit cell.

Band theory is able to provide an explanation of these differences. Electrons in the free electron theory have discrete energies however in band theory the available energy states form bands which are separated by regions in which no electron orbitals exist. These forbidden regions are called band gaps. In insulators, the band gap between the valence and conduction energy bands is very large. In conductors, the

valence and conduction bands overlap, and in semiconductors there is a small band gap between the valence and conduction band which allows for unique thermal and optical excitations. The band structure of graphene is very unique because its valence and conduction band are symmetrical shaped cones which connect at a Dirac point. This point subsequently means that graphene does not contain a band gap.

### *2.1.4 Graphene Field Effect Transistors*

The Fermi energy level is an important consideration when discussing band theory and GFET devices. The Fermi level quantifies the highest occupied electron energy level at absolute zero temperature. The Fermi level can lie inside a band gap (where no energy levels exist). In this case the Fermi energy, $E_F$, is used in the Fermi-Dirac distribution to calculate the probability that nearby energy levels are thermally populated.

$$f(E) = \frac{1}{e^{(E-E_F)/k_B T} + 1} \tag{2.11}$$

The quantity $k_B$ is Boltzmann's constant, $T$ is the absolute temperature, and $E$ is the energy level of the particle. For $E - E_F < 0$, in the limit $T \to 0$, the argument in the exponential becomes minus infinity and makes the exponential term zero. Hence the probability, $f(E)$, that nearby energy levels less than the Fermi energy are thermally populated is 1 at $T = 0$. For $E - E_F > 0$, in the limit $T \to 0$, the argument in the exponential becomes infinity and makes the exponential term infinite. Hence the probability, $f(E)$, that nearby energy levels greater than the Fermi energy are thermally populated is zero at $T = 0$.

In an intrinsic semiconductor like undoped silicon, the Fermi level is halfway between the valence and conduction bands. This means that at absolute zero temperature there are no electrons in the conduction band however at finite temperatures some electrons have energies higher than the Fermi level and can reach

the conduction band. The Fermi level in a GFET device can essentially be shifted by applying a bias across one of the electrodes and the back gate.

As we have addressed previously, the graphene in a GFET device acts as the semiconducting channel across two electrodes which all lie atop an electrical insulator such as $SiO_2$. When a bias is placed across the back-gate and the source electrode, the device behaves like a parallel plate capacitor (Fig 2.2). For a device with parallel plates both of area $A$ and separated by distance $d$, the capacitance is

$$C = \epsilon_r \epsilon_o \frac{A}{d} \tag{2.12}$$

In the GFET device, $A$ is the area of the electrode, $d$ is the thickness of the $SiO_2$ dielectric, $\epsilon_r$ is the relative static permittivity or the dielectric constant, and $\epsilon_o$is the permittivity of free space.

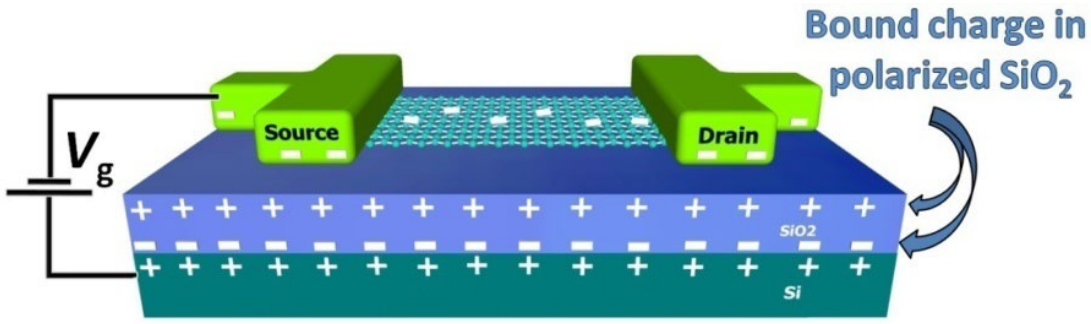


**Figure 2.2** Schematic of a GFET acting as parallel plate capacitor.

When we apply a back-gate voltage we are effectively creating a potential drop between the graphene and the substrate. This results in a tunable shift in the Fermi level of our device and allows us to dope the graphene without physically altering the sample. This Fermi level shift dopes the graphene and is able to change it from either p-type or n-type. This shift also leads to a very interesting and unique current vs. back gate voltage curve (Fig 2.3). When the Fermi level coincides with the energy of the Dirac point the graphene is neutral and conductivity is a minimum. If the Fermi level

is greater than zero the conduction is by electrons, or n-type. If the Fermi level is less than zero the conduction is by holes, or p-type. Doping can also occur as a result of impurities such as oxygen or nitrogen present in the graphene lattice. Importantly for this project, doping can also be induced by surface contaminants. These impurities make the graphene n-type or p-type and shift the charge neutrality point or Dirac point away from zero.

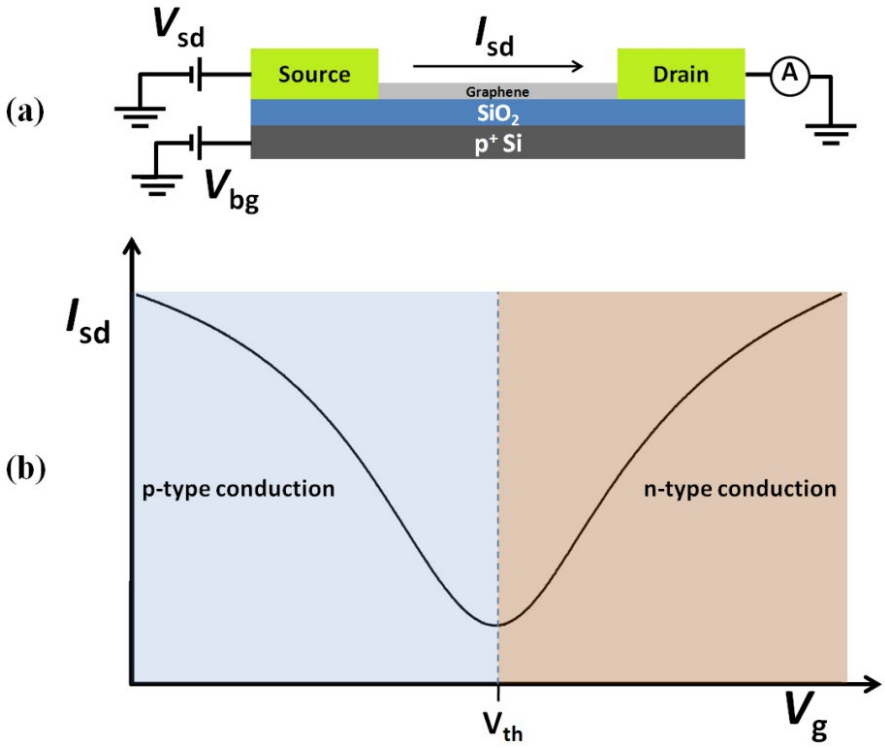


**Figure 2.3 (a)** Schematic of a GFET device. **(b)** *I*-$V_g$ curve showing regions of hole and electron conduction. The voltage threshold ($V_{th}$) is the charge neutrality point or Dirac point, where the conductivity in the graphene sheet is a minimum.

### *2.1.5 Graphene Field Effect Transistors as Biosensors*

By applying a liquid-gate voltage to an electrolytic solution in contact with the surface of graphene, we can essentially make a GFET device behave as it does in open air. Depending on the electrochemistry of the reference electrode, a certain applied voltage will put graphene in the neutral charge state. If the liquid-gate voltage is greater than or less than the charge neutrality point then positive or negative ions are concentrated

at the sample surface and we are able to create a potential drop across the graphene surface and the liquid-gate electrode, effectively producing a liquid-gated capacitance. The total capacitance can be modeled as two capacitors in series

$$\frac{1}{C_T} = \frac{1}{C_Q} + \frac{1}{C_G} \tag{2.13}$$

where $C_Q$ is the quantum capacitance and $C_G$ is the geometrical capacitance. The geometrical capacitance is given by eq. (2.12) where $d$ is a new quantity called the Debye length. The quantum capacitance is related to the Fermi level shift and subsequently, the potential drop across this capacitance controls the Fermi level shift.[34]

The GFET biosensor's capabilities are limited by a few factors. One of those factors is the Debye length. This is the distance away from the graphene surface for which the GFET device is able to screen a charge. The Debye screening length in an electrolyte is

$$\lambda = \sqrt{\frac{\epsilon\, \epsilon_0 k_B\, T}{2\, n\, Z^2 e^2}} \tag{2.14}$$

where $n$ is the bulk concentration of ions in the solution, $Z$ is the charge of the ion, and $e$ is the charge of an electron. The Debye length can be approximated as

$$\lambda \approx 0.96 \text{ nm} \sqrt{\frac{0.1 \text{ M}}{[\text{ c }]}} \tag{2.15}$$

where [ c ] is the molar concentration of the salt solution. In this project we are non-covalently binding a pyrene linker molecule to the graphene surface. The pyrene linker then binds to a thrombin aptamer molecule which specifically binds to thrombin

protein. The pyrene and aptamer together are approximately 3-5 nm, so we essentially need a solution of concentration which gives a Debye length greater than 5 nm so the GFET device can screen and detect a charge when the thrombin protein binds to the aptamer.

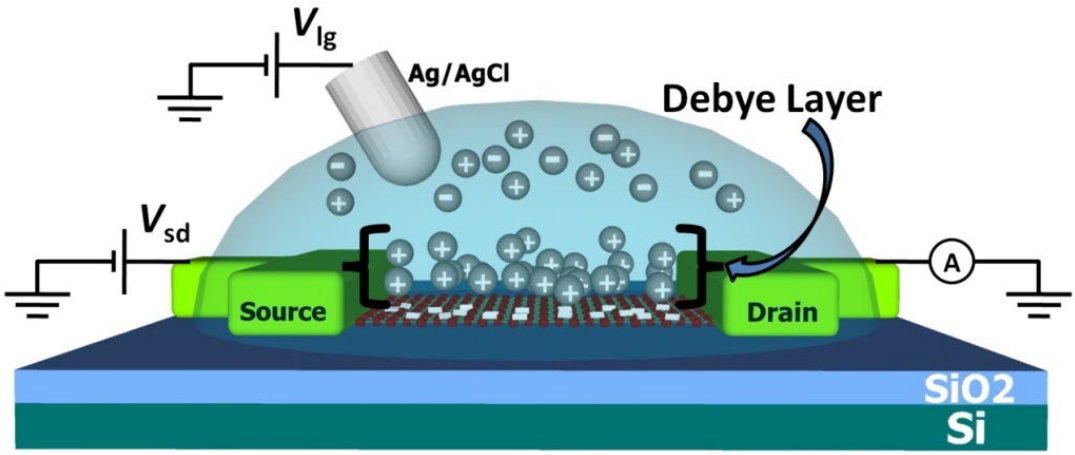


**Figure 2.4** Schematic of a liquid-gated GFET device. Positive (or negative depending on the applied liquid-gate voltage) ions near the surface of the graphene make up the Debye layer.

The GFET biosensing device is highly sensitive to any fluctuations in local charge distributions. It has been shown that charge trapping in GFET devices can be detrimental to its performance.[35] Charge trapping occurs when charges migrate into the dielectric substrate. This results in a loss of mobility in the graphene sheet and creates unwanted low frequency noise. Recently, Heller et al. have shown that for low carrier densities the noise in a liquid-gated GFET device is dominated by charge fluctuations near the graphene sheet and that the power of the charge noise in these devices scales inversely with the device area and number of graphene layers.[36]

Another factor that limits a GFET biosensing device is Faradaic currents. These currents are created by the reduction or oxidation of molecules at the liquid-metal interface. The result is a charge transfer occurring at the electrode surface creating unwanted currents in the device. A measurement of these currents in the window of the liquid-gate voltage is necessary to make sure that they are not dominant over

currents associated with the graphene sheet. In general, Faradaic currents should be less than 1 nA. For the experiment presented in this paper, Faradaic currents of 1 nA are approximately 3 orders of magnitude smaller than currents in the graphene, and therefore negligible. Faradaic currents can be alleviated by passivation, which entails coating the top of the electrodes with a layer of oxide to reduce the interaction between the electrode surface and the solution.

## 2.2 Raman Spectroscopy

The carbon atoms in a graphene lattice can be modeled as masses on springs where the mass is the mass of the carbon atom and the spring is the bond between atoms. When an incident photon strikes the graphene lattice an inelastic collision occurs and energy is lost from the photon and transferred into the vibration of the lattice. This amount of energy lost into the vibration of the graphene lattice can be quantified by calculating the energy difference between the incident and reflected photon. This process is called Raman spectroscopy and can tell us specific information about the structure of a graphene lattice by simply observing the energy(ies) of reflected photons.

A Raman spectral analysis of a graphene lattice can reveal information about the number of graphene layers present,[37] defects in the lattice,[38] the amount by which the graphene may be doped,[39] and the angle at which double stacked graphene is rotated.[40] There are three main peaks in the Raman spectra of graphene which are typically labeled D, G, and 2D (Fig 2.5).

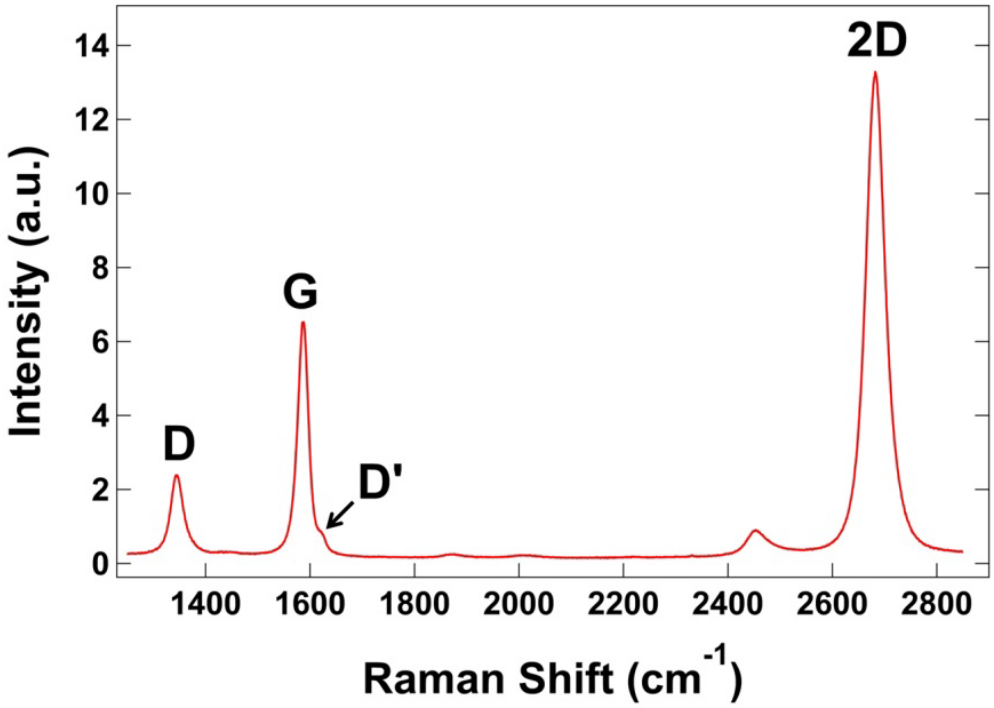


**Figure 2.5** Raman spectrum of graphene on a $Si/SiO_2$ substrate.

### *2.2.1 The G Band*

The G peak or band is derived from the motion of two adjacent carbon atoms in the plane of a graphene lattice,[37] and is a doubly degenerate phonon mode with $E_{2g}$ symmetry at the Brillouin zone center.[41] When carbon bonds are stretched by strain induced from interactions from a substrate or other graphene layers, graphene's hexagonal structure becomes asymmetrical.[42] This G band is therefore highly sensitive to strain effects in $sp^2$ carbons. The G band is observed both in graphene and in planar lattice vibrations in highly ordered pyrolytic graphite which exhibit an optical response at 1582 $cm^{-1}$.[38] In single layer graphene the G band is shifted up in frequency to approximately 1580 $cm^{-1}$.[37,43]

Recent studies using GFET devices have shown that Raman spectroscopy is a valuable tool to characterize doping levels by observing the frequency and width of the G band.[44-46] These studies induced electron and hole doping in graphene by

varying the gate voltage and observing the corresponding Raman spectra for each gate voltage. Shifting the Fermi energy level from induced doping results in a change in the equilibrium lattice parameter, and the excess charge results in an expansion or contraction of the graphene lattice.[45] As we discussed previously, the G band is sensitive to any strain induced on $sp^2$ carbons and subsequently results in a shift in frequency and width.[45] Other groups have discovered similar shifts in frequency of the G band due to doping from aromatic molecules,[47] and from doping along the edges of graphene.[39]

### *2.2.2 The D Band*

The edges of graphene typically contain defects and are characterized by a D band in the Raman spectrum around approximately 1350 $cm^{-1}$.[43] Disorder induced Raman features can also appear as a second band typically labeled D' and occur around approximately 1620 $cm^{-1}$.[41] D and D' bands have been observed on graphene lattices after inducing defects by the deposition of $SiO_2$,[48] and also by bombardment of the lattice with electrons,[49] and $Ar^+$ ions.[50] The causes of D and D' bands are theorized to be from vacancies, dislocated or dangling bonds in the graphene lattice,[48] and from certain crystallographic orientations of the graphene edges.[51] Raman spectroscopy has been valuable in characterizing defect and edge features in graphene as well as graphitic materials in general.[41,50,52]

In 1970, Tuinstra and Koenig quantified the evolution of disorder in crystalline $sp^2$ clusters by using a ratio of the intensities of the D and G bands.[53] They found that the ratios of the intensities of the D and G bands follow the relationship

$$\frac{I_D}{I_G} = \frac{C(\lambda)}{L_a} \tag{2.16}$$

where $L_a$ is the crystalline size, and $C(\lambda)$ is a proportionality constant which depends on the excitation laser wavelength.[53] A new model proposed by Lucchese et al. uses

the ratio $I_D/I_G$ to quantify the density of defects, or the average distance, $L_D$ between defects in graphene.[50] This model shows that the ratio $I_D/I_G$ increases with increasing $L_D$ up to approximately 4 nm then decreases exponentially for $L_D$ > 4 nm.[50] This behavior is explained by the competition between two disorder mechanisms, and their model can be used to quantify the relative importance of each mechanism.[50]

### *2.2.3 The 2D Band*

Similar to the G band, the 2D band is present in all types of $sp^2$ carbon materials and displays a strong feature in the Raman spectra around approximately 2700 $cm^{-1}$.[37,38,43] The D and 2D bands are activated by a double resonance (DR) process which involves the coupling of two phonons with opposite wavevectors.[37,54] This DR process results in a dispersive relationship which consequently causes the 2D band to be dependent on perturbations to the electronic and/or phonon structure of graphene and exhibit a strong frequency dependence on the excitation energy from the laser.[37,54,55]

Recent work has shown that the 2D band can be used to identify the number of layers present in AB stacked graphene.[43,54] As the number of layers increases the DR processes increase until the shape of the 2D band eventually converges to that of bulk graphite which results in two peaks.[54] It should be noted that this method for identifying the number of layers is only well established for samples made from mechanical exfoliation of HOPG which predominately have AB stacking, however this is not necessarily the case for graphene obtained from other methods which may have layers that are rotationally random with respect to one another.[40,54]

A common misconception is to assume that a large ratio between the intensities of the 2D and G bands is a good method to distinguish between single or multilayer graphene. Recent reports have observed the Raman spectra for $SiO_2$ doped single layer graphene,[48] double-stacked rotated graphene,[40] and single layer graphene that has been doped via a gate voltage,[45] which show that the $I_{2D}/I_G$ ratio and the position of the G peak should not be used to estimate the number of graphene layers. This is contrary to what was previously suggested by Gupta et al.,[56] and Graf et al.[57]

The 2D band, like the G band, is sensitive to doping,[45,46,58] however the bands show different dependencies on doping levels.[45,46] These dependencies show that the ratio $I_{2D}/I_G$ is a strong function of doping induced by a gate voltage and is therefore an important parameter to estimate doping densities in graphene.[45]

CHAPTER 3

# Methods

## 3.1 Graphene Growth

CVD grown graphene was used for the experiments performed in this paper and was obtained via a CVD system at Oregon State University and from Nanotechnology Biomachines, Inc.

The CVD growth of graphene at Oregon State University was performed under vacuum in a 4 inch furnace. A high purity (99.8% trace metals basis obtained from Alfa Aesar) copper foil was used as a substrate for the deposition of graphene. The copper foil was prepared by a "standard" and "pita-pocket" method. The standard method is simply a square or rectangular section of copper small enough to be inserted into the 4-inch quartz tube. These squares were typically 2 x 2 inches. The pita-pocket method uses a rectangular piece of copper that is folded and sealed on all but one side creating a pocket for a second piece of copper to be inserted inside of it. The remaining side is then sealed enclosing the copper foil.

Before inserting the copper foil, the furnace pressure was pumped down to ~$10^{-6}$ Torr and flushed with a mixture of Ar and $H_2$. This ensures that the system is free of contaminates and leaks before the growth process. We then raised the growth chamber pressure to atmospheric pressure and inserted the copper foil into the center of the quartz tube. The system was sealed and the pressure inside the growth chamber was pumped down to ~$10^{-6}$ Torr. All three stages of the growth process are done under high vacuum at ~$10^{-6}$ Torr. A typical anneal was performed at 1000 °C while flowing ~30–70 SCCM of $H_2$ for 60 minutes. This removes oxygen and other contaminates from the growth chamber and copper foil before the growth process. The growth stage was performed at 1000 °C while flowing ~50–70 SCCM of $H_2$ and 2 SCCM Methane for 20 minutes. The furnace was then cooled to 200 °C while flowing the same growth gases.

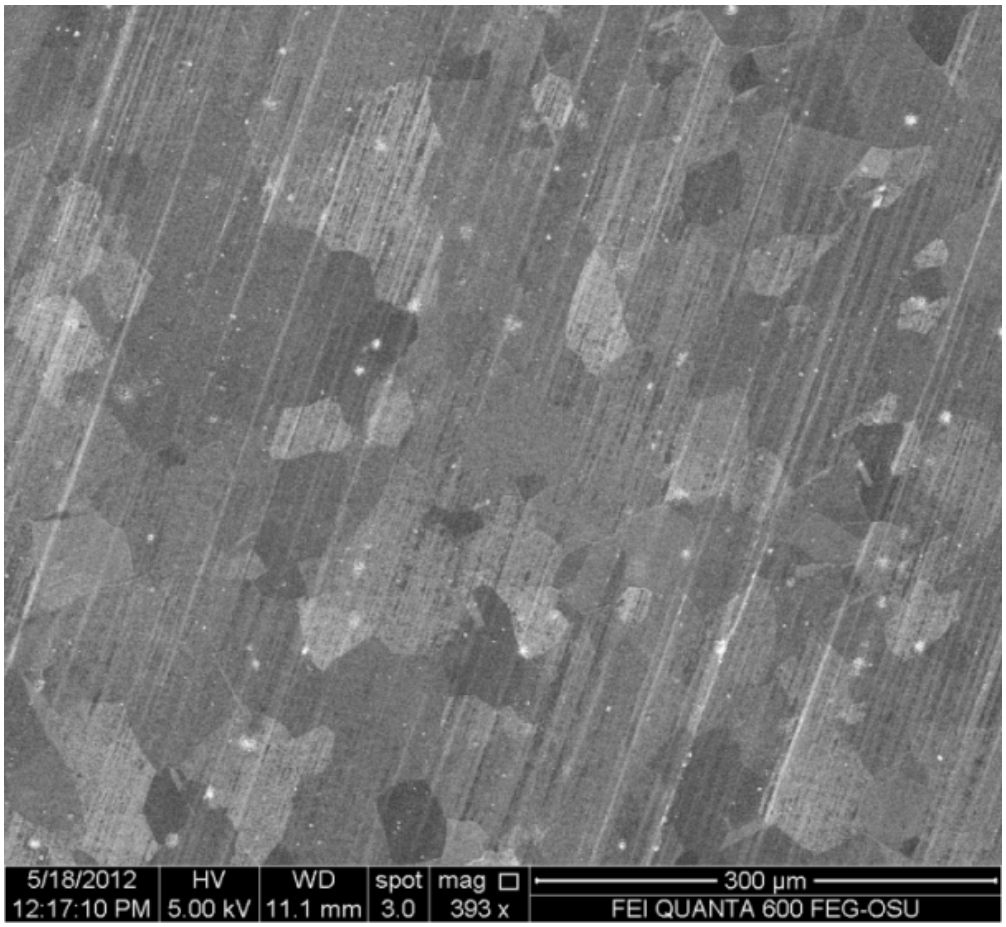


**Figure 3.1** SEM image of graphene on copper foil. This graphene was obtained from Nanotechnology Biomachines, Inc.

## 3.2 Fabrication of Graphene Field Effect Transistors

### *3.2.1 Graphene Transfer Process*

After the growth process the copper foil was cut into 2 x 2 cm squares. One side of the copper was spun coated at 4000 rpm for 1 minute with 2% polymethyl methacrylate (PMMA) in a solution of Anisole. The samples were then placed into a copper etchant (type CE–200) bath with the PMMA side facing upward for at least 12 hours. The etchant removes the bottom layer of graphene and copper foil, leaving the top layer of graphene and PMMA. A diluted hydrochloric acid bath was also used as an etchant. Graphene samples were placed a bath consisting of DI water, HCl, and $H_2O_2$ with a 45:5:1 ratio for 12 hours. This etchant resulted in tearing a majority of the graphene

samples. A shorter time period, or a more diluted concentration of HCl and $H_2O_2$ might result in less tears.

After etching, the samples were transferred to 3 separate deionized (DI) water baths for approximately 30 minutes each, then to a final DI water bath for at least 12 hours. A fresh silicon wafer was used to transfer the samples. After each transfer the silicon wafer was cleaned with acetone, isopropyl alcohol, DI water, and then dried with ultra-high purity $N_2$. All glassware used in the transfer process was cleaned using the same process.

The silicon substrates used in the biosensing experiments were obtained from WRS Materials and were p-doped with a 500 nm top layer of thermal oxide. The $Si/SiO_2$ wafers were cut into 2 x 2 cm squares, large enough to accommodate the metal electrode pattern. The $Si/SiO_2$ wafers were cleaned with acetone, isopropyl alcohol, DI water, and then dried with ultra-high purity $N_2$ before the transfer process. The graphene with PMMA was then transferred to the $Si/SiO_2$ wafer. The wafer was dried from the center of the graphene outward, using low pressure ultra-high purity $N_2$ to aid in the adhesion of the graphene to the substrate. The samples were placed in a 1 inch furnace in open air at 30 °C for 4 hours before the removal of PMMA to ensure that the graphene was properly adhered to the substrate. PMMA was removed in the same 1 inch furnace in open air at 350 °C for 4 hours.

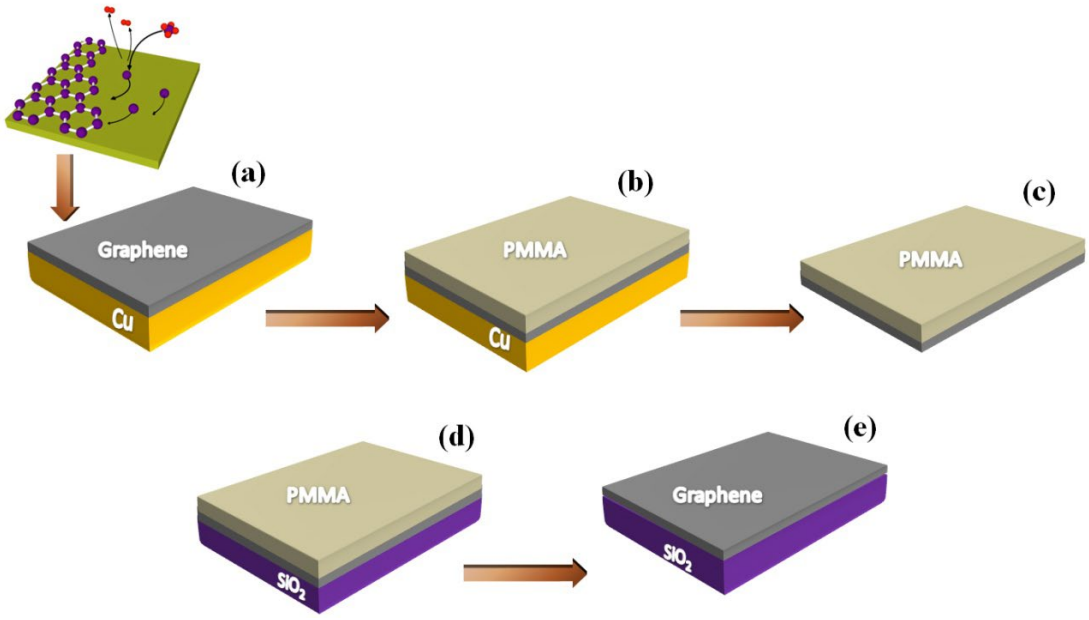


**Figure 3.2** Graphene transfer process. **(a)** Graphene is grown via CVD on copper foil. **(b)** PMMA is spun on top of graphene. **(c)** Copper foil is removed with an etchant bath. **(d)** Graphene with PMMA is transferred to $Si/SiO_2$ substrate. **(e)** PMMA is removed.

### *3.2.2 Device Fabrication*

The scale of the devices required the use of alignment marks to ensure that graphene would be properly aligned across the electrode gaps. Alignment marks were pattered onto the $Si/SiO_2$ substrate using photolithography and a metal deposition. The samples were spun coated with LOR3A at 4000 rpm for 45 seconds then baked on a hot plate for 4 minutes at 190 °C. The LOR3A under layer aids in the process of metal lift off. S1813 photoresist was then spun coated at 4000 rpm for 30 seconds and baked on a hot plate for 90 seconds at 115 °C. A contact aligner was used along with an appropriate alignment mark mask to expose the samples for 4.5 seconds. The samples were developed in AZ–726 for 90 seconds and rinsed in a short DI bath. 20 nm of chrome was deposited using an electron beam (e-beam) metal evaporator. The samples were then placed in PG remover for at least 12 hours at 70 °C to remove any photoresist and excess metal. Each sample was cleaned with PG remover, isopropyl

alcohol, DI water, and then an ultra-high purity $N_2$ blow dry after they were taken out from the PG remover.

The second step in the process is to etch away all of the graphene from the substrate except where it is located across the electrode gaps. The photolithography for this step is identical to the alignment mark procedure except for the under layer, and the type of mask used. In lieu of LOR3A, P20 primer was spun coat at 4000 rpm for 30 seconds. An appropriate mask that was designed to etch away the graphene was used in the contact aligner during the exposure. After developing in AZ–726 for 90 seconds and rinsing in a short DI bath, the samples were ready to be placed in an $O_2$ plasma etcher. The plasma etching chamber was cleaned by running the system empty for 4 minutes. The samples were then placed in the plasma etcher for 4 minutes.

The last step in the fabrication process is the deposition of the metal electrodes. The photolithography and metal deposition procedures for this step are identical to the alignment mark procedure except for the type of mask and metal used. An appropriate mask designed for electrodes was used in the contact aligner. During the e-beam metal deposition a 1.5 nm layer of chrome was deposited first and acted as the sticking layer. 30 nm of gold was then deposited on top of the chrome to create the bulk of the metal electrodes.

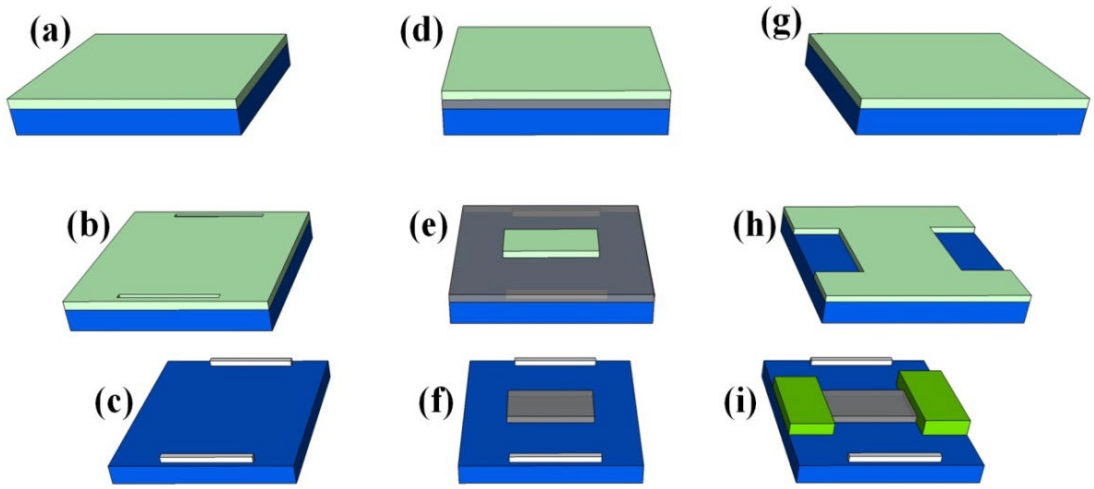


**Figure 3.3** Device fabrication process for biosensing devices. **(a)** Photoresist is spun onto $Si/SiO_2$ substrate. **(b)** The photoresist is patterned for alignment marks and developed. **(c)** Chrome alignment marks are deposited via e-beam metal evaporation and remaining metal and photoresist are stripped. **(d)** Graphene is transferred to $Si/SiO_2$ substrate, PMMA is removed, and photoresist is spun on top of graphene. **(e)** Photoresist is patterned and developed for graphene etching. **(f)** Graphene is removed via $O_2$ plasma etching, and remaining photoresist is stripped. **(g)** Photoresist is spun onto sample. **(h)** Photoresist is patterned for electrodes and developed. **(i)** Gold electrodes are deposited via e-beam metal evaporation and excess metal and photoresist are stripped.

A preliminary and secondary set of devices were fabricated for the experiments performed in this paper. The secondary sets of devices were used in the biosensing experiments. In the preliminary set, alignment marks were patterned after graphene was transferred to the $Si/SiO_2$ substrate. The graphene used for the preliminary devices was grown via CVD at Oregon State University, and the graphene width across the 4 μm electrode gaps was 32 μm. For the biosensing devices, contamination of the graphene surface through an extra photolithography step was avoided by patterning alignment marks on the $Si/SiO_2$ substrate before the graphene was transferred. The graphene used for the biosensing devices was obtained from Nanotechnology Biomachines, Inc., and the graphene width across the 4 μm electrode gaps was reduced to 3 μm.

## 3.3 Functionalization of Thrombin Aptamer

Amine reactive 1–pyrenebutanoic acid succinimidyl ester (PBASE) was obtained from Invitrogen and functioned as the linker molecule between the graphene surface and thrombin aptamer. PBASE has been used in the past for both carbon nanotube[15] and graphene[10] functionalization. The PBASE non-covalently binds to the graphene surface via $\pi$ stacking. GFET devices were immersed in a methanol solution of 5mM PBASE for 1 hour at room temperature to achieve functionalization with the graphene surface. The devices were rinsed with methanol then immersed in a 20 mM 2–morpholinoethanesulfonic acid (MES) solution with 1 nM thrombin aptamer for 12 hours at room temperature. The custom synthesized thrombin aptamer DNA oligonucleotide was obtained from Integrated DNA Technologies and the base sequence was 5'–/5Amino C6/GGT TGG TGT GGT TGG–3'. The oligonucleotide came synthesized with an amine group which reacts with the amine-reactive PBASE molecule. A final rinse with 20 mM MES solution at room temperature was performed to remove any reactive groups that may have remained on the graphene surface. The thrombin protein from human plasma was obtained from Sigma–Aldrich.

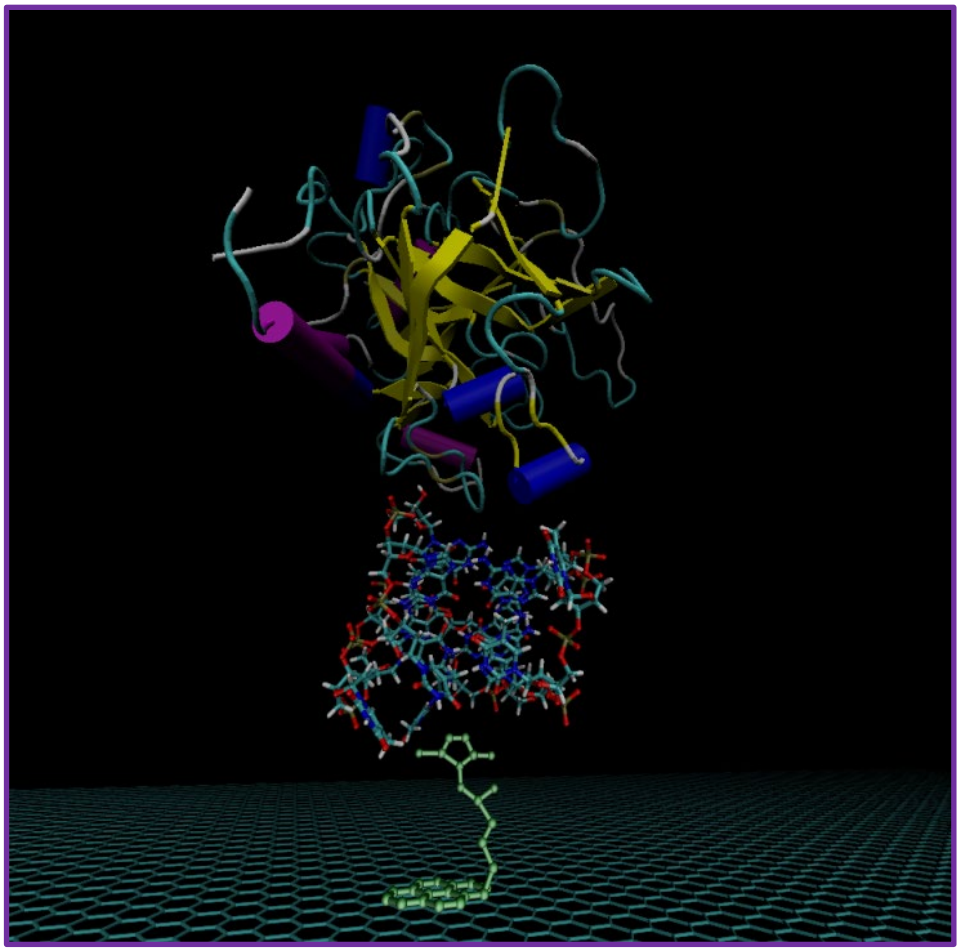

**Figure 3.4** PBASE (green) on graphene sheet, thrombin aptamer (middle) and cartoon rendering of thrombin protein (top).

## 3.4 Electrical Measurements and Microfluidics

Electrical measurements were performed inside a Faraday cage for the reduction of noise. All probe needles were insulated and had their shielding grounded to a common point. This common point was also the location for all other ground connections. The source-drain voltage was supplied by a Stanford Research Systems (SR570) pre-amplifier. The source-drain voltage for all measurements performed in this paper was 25 mV. The current was measured with the SR570 current pre-amplifier which converted the current to a voltage and output the signal to a National Instruments

DAQ (NI USB 6251) analog to digital converter. Liquid and back-gate voltages were supplied with a Yokogawa GS200 DC voltage/current source.

Thrombin protein was delivered to the GFET device via a microfluidic mass-flow system. The microfluidic channel was made from polydimethylsiloxane (PDMS) and created a temporary seal which enclosed the electrode gaps. An $N_2$ gas cylinder provided pressure to a syringe full of solution which pushed the fluid through the microfluidic channel. The PDMS stamp and Ag/AgCl top-gated reference electrode were held in place with an acrylic fixture.

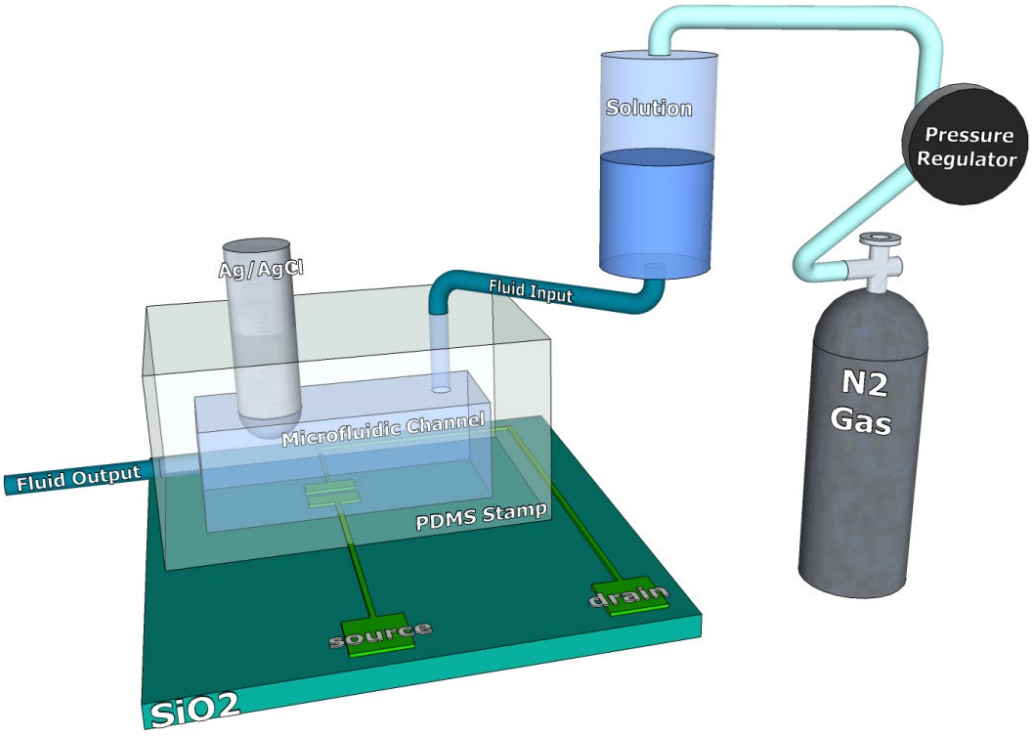


**Figure 3.5** Microfluidic experimental setup.

CHAPTER 4

# Results and Discussion

## 4.1 Preliminary Devices

Electrical measurements were taken on the preliminary set of devices to observe their electrical characteristics in both open air and liquid environments, and to determine if they were suitable for a biosensing experiment.

All measurements taken in open air were back gated. Initial electrical measurements showed a back gate response in open air. The charge neutrality point was beyond $V_{bg}$ = +200 V, which suggested that the device was heavily p-doped. The anomaly in the transistor curve shown in Fig 4.1 (a) around the range of 180–200 V was believed to be an effect of the voltage amplifier and not related to the device's electrical characteristics. The open-air gate response also shows evidence of hysteresis. Hysteresis phenomena are thought to be the result of charge trapping,[59] or altering the surface dipole moment near graphene which may occur from tape residues,[60] atmospheric water,[60,61] or e-beam resist.[59] In later AFM scans we observed a residue on the surface of our graphene which was believed to be from the photolithography processes. The hysteresis we observed may therefore be a result of that residue, or from charge trapping near the graphene.

To measure devices in liquid, a PDMS stamp was fitted to the GFET device as described in section 3.4. The device was flushed with ethanol, and then a PBS buffer (pH 7) was added to observe the liquid gated response. Faradaic currents were measured and were less than 1 nA. The Faradaic currents dictate the range of the liquid gate voltage. Beyond these ranges, Faradaic currents are greater than 1 nA and can no longer be neglected in comparison to the current in the graphene channel. The charge neutrality point was outside the range of the liquid gate voltage, suggesting that our device was heavily p-doped. Compared to the open-air measurements, there was higher conductance, and a larger on/off ratio (data not shown).

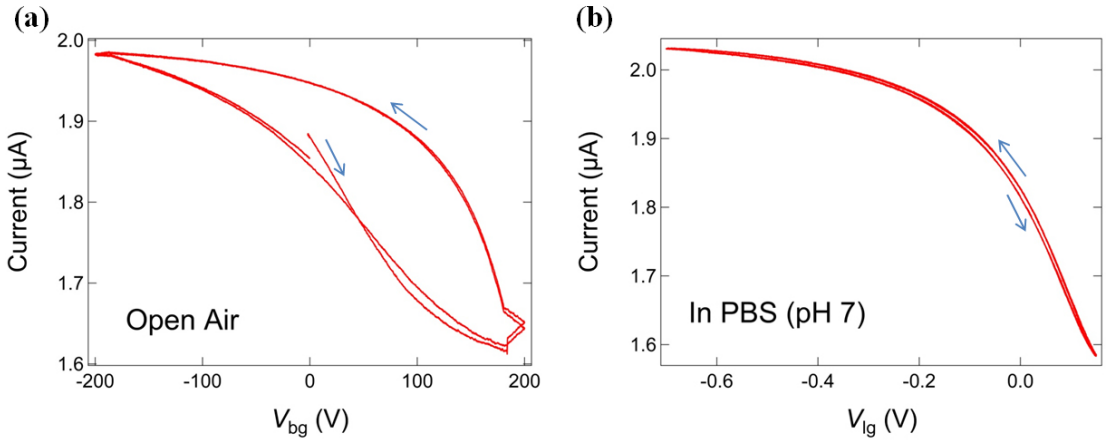


**Figure 4.1** Electrical characteristics of a preliminary GFET device in open air **(a)** and in a PBS buffer **(b)**. The blue arrows indicate the direction the gate voltage was swept.

### *4.1.1 Effects of an Anneal Process*

A preliminary GFET device was annealed to clean the graphene surface and observe any changes in its electrical characteristics. The GFET was annealed at 500 °C while flowing 1 SLM Ar and 0.45 SLM $H_2$ for 20 minutes. A gate response was observed in open air before the anneal (Fig 4.2a). We observed a lower on/off ratio compared to the open-air gate response of the GFET in the previous section. The charge neutrality point was outside the range of the gate voltage, suggesting that the device was heavily p-doped. After the anneal, the device was fitted with a PDMS stamp, flushed with ethanol, and immersed in a PBS buffer (pH 7). Faradaic currents were measured and were less than 1 nA. The GFET device exhibited a gate response, however, the charge neutrality point was beyond the range of the liquid gate voltage. The on/off ratio of the liquid gated annealed device was much smaller compared to the open-air electrical response.

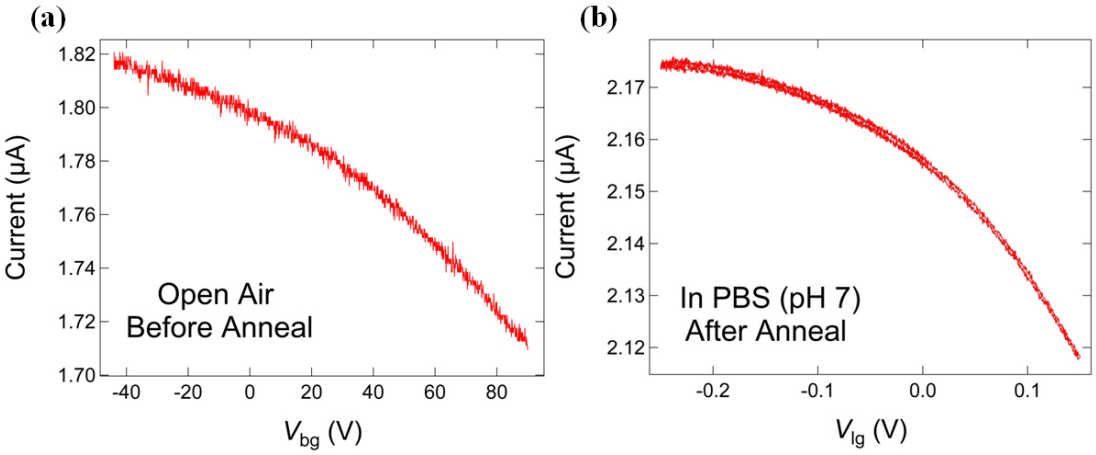


**Figure 4.2** Electrical characteristics of a preliminary GFET device in open air before anneal **(a)** and in a liquid environment after an anneal **(b)**.

Based on these results it was difficult to say whether an anneal improved the electrical characteristics of our devices. An important factor in a biosensing experiment is to the see the shift in the charge neutrality point before and after a molecule has bound to the surface of the graphene sheet. Therefore, it was disappointing that we could not access the charge neutrality point in our preliminary devices.

We were unable to see a charge neutrality point in a liquid environment in all the experiments performed on our preliminary devices. Therefore, we decided to make a second set of devices, revise the photolithography process, and modify one step in the process. In this second set of devices, the alignment marks were deposited on the $Si/SiO_2$ substrate before transferring the graphene. This limited the graphene's exposure to photolithography steps. Photoresist only contacts the graphene twice instead of three times, thus limiting the amount of residue that may contaminate the graphene surface.

## 4.2 Biosensing Devices

Electrical measurements were taken on the second set of GFET devices to observe their electrical characteristics and determine if they were suitable for biosensing experiments. The GFET device was back gated and showed a response similar to what

we observed previously. The charge neutrality point was still beyond the range of the gate voltage; however, the on/off ratio was twice as high as observed with the preliminary set of GFET devices (Fig 4.3a). There was evidence of hysteresis, suggesting that the graphene may have had residue on its surface.[59]

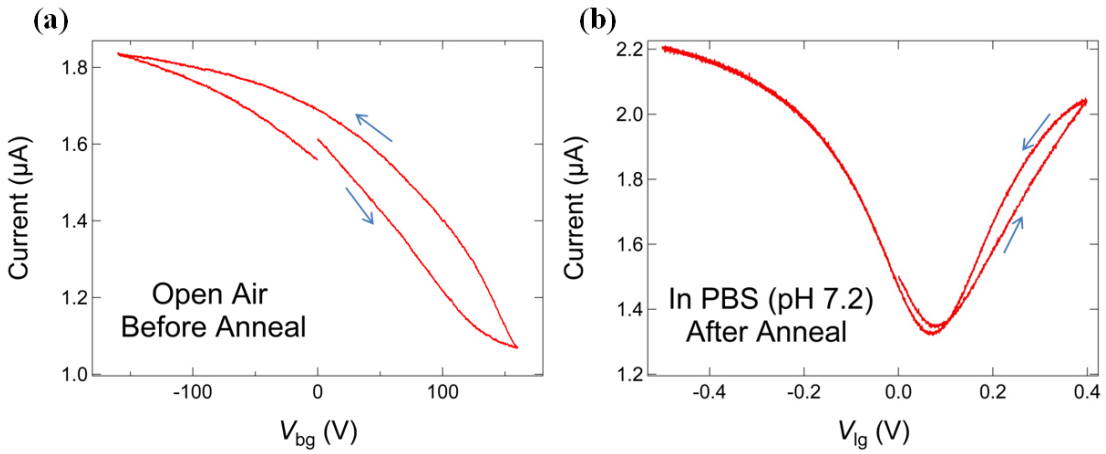


**Figure 4.3** Electrical characteristics of a biosensing GFET device in open air **(a)** and in a PBS buffer **(b)**. The blue arrows indicate the direction the gate voltage was swept.

The device was annealed before it was immersed in a liquid environment. The GFET was annealed at 400 °C while flowing 0.85 SLM Ar and 0.95 SLM $H_2$ for 1 hour. The GFET was then fitted with a PDMS stamp, flushed with ethanol, and immersed in a PBS buffer (pH 7.2). Faradaic currents were measured and were less than 1 nA. The liquid gated GFET device exhibited a gate response with a charge neutrality point within the liquid-gate voltage range. This data suggested that these devices were suitable for a biosensing experiment.

### *4.2.1 Effects of an Anneal Process*

A fresh device from the same batch was chosen to attempt a thrombin biosensing experiment. First, the GFET was annealed at 400 °C while flowing 0.85 SLM Ar and 0.95 SLM $H_2$ for 1 hour. The intention of this anneal was to improve the thrombin aptamer functionalization scheme by cleaning the surface of the graphene.

An AFM image of the graphene channel in the GFET device before the anneal shows that the average height of the graphene surface above the substrate is ~2–3 nm. The corresponding height profile shows that there are large ~1–4 nm structures on the graphene surface. There is also a fencing like structure ~4 nm in height which can be observed on the edges of the graphene in the AFM image. This fencing structure is believed to be from a combination of the graphene plasma etching, and electrode photolithography processes.

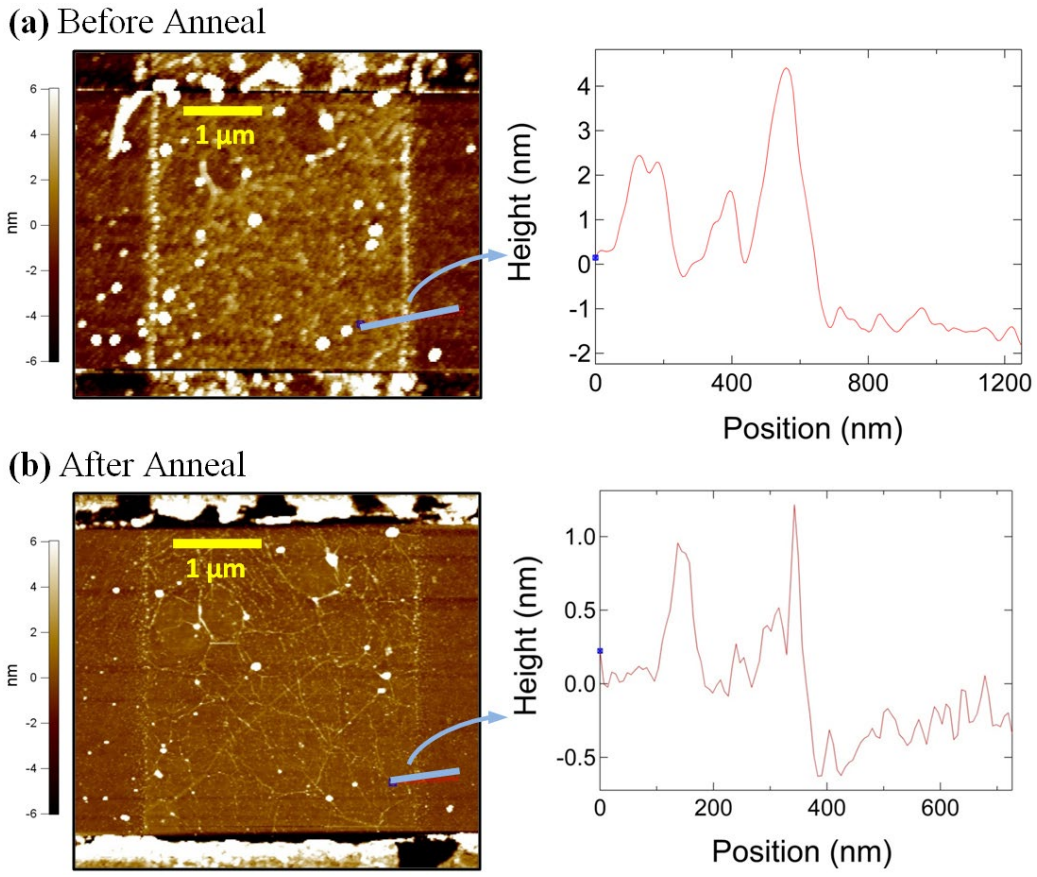


**Figure 4.4 (a)** AFM image of graphene channel in GFET before anneal and corresponding height profile marked by blue line. **(b)** AFM image of graphene channel in GFET after anneal and corresponding height profile marked by blue line. The electrodes are located in the top and bottom ~0.5 µm portions of both AFM images. A color map of the height range is located at the left of each AFM image.

The AFM image of the graphene channel after the anneal shows a drastic improvement in height characteristics. A height profile was taken at the approximate location of the height profile from the pre-anneal AFM image and shows that the average height of the graphene surface above the substrate after the anneal was reduced to ~0.5 nm. The height profile also shows that the fencing structure surrounding the graphene edges was reduced by as much as 3 nm. Comparing the two AFM images we can see that there was a thin coat of residue on the graphene surface before the anneal, and that most of this residue was removed after the anneal.

Raman spectra were attained for the graphene channel in the GFET device before and after the anneal. A 532 nm laser with an excitation energy of 2.33 eV was used to record the spectra in ambient light conditions. The laser was positioned in the same spot in the graphene channel before and after the anneal. The Raman spectra suggest that the graphene in the GFET channel is most likely double or multi-layer.[40,52]

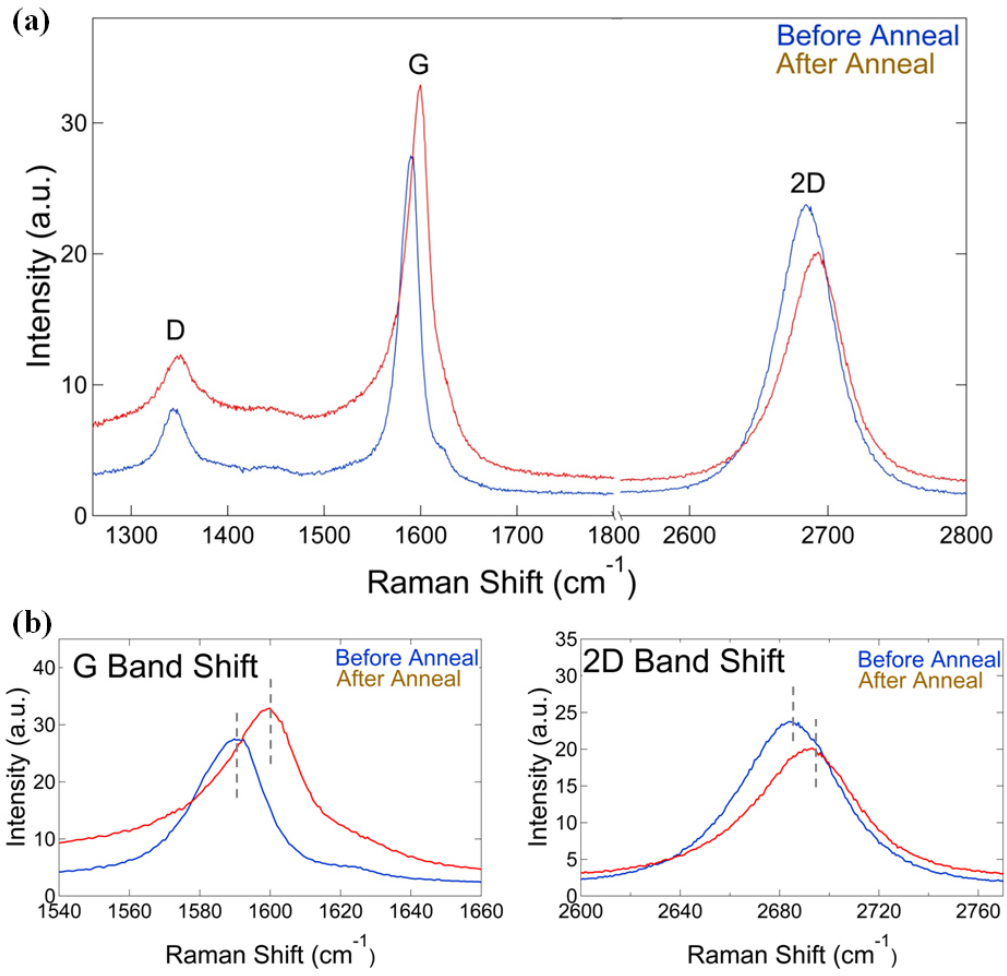


**Figure 4.5 (a)** Raman spectra of graphene channel in GFET device before (blue) and after (red) an anneal. **(b)** The G and 2D band shifts resulting from the anneal process.

Recent studies performed on electrochemically top gated GFETs have shown that the positions of the G and 2D bands, as well as their FWHM exhibit clear dependencies on hole and electron doping.[45] The Raman spectra for the graphene channel in our GFET device show that there was a significant shift in the positions of the G and 2D bands. The G peak position in our Raman spectra increases from 1588 $cm^{-1}$ to 1597 $cm^{-1}$, and the FWHM decreases in line width from 26 to 24 after the anneal process. This shift in the position and stiffening of the G peak are characteristic of doping effects,[45] however cannot be used alone to distinguish between electron and hole doping.[45]

As experimentally determined by Das et al., the position of the 2D peak decreases for an increasing electron concentration and therefore allows the 2D peak position to distinguish between electron and hole doping.[45] The 2D peak position in our Raman spectra increases from 2684 $cm^{-1}$ to 2690 $cm^{-1}$, suggesting that the electron concentration decreased, resulting in a device that was more p-type after the anneal.

The ratio of the 2D and G peak intensities also show a clear dependence on electron concentration.[45] This ratio decreases from 0.88 to 0.61 after the anneal and suggests that the anneal was responsible for changing the doping level of the device. [45] The ratios of the D and G peak intensities only varied slightly from 0.30 to 0.37, suggesting that no significant defects were introduced into the graphene lattice during the anneal process.[50]

### *4.2.2 AFM Observation of Thrombin Aptamer Functionalization*

After the anneal of the GFET as described in section 4.2.1, PBASE and thrombin aptamers were functionalized on the graphene surface using the methods described in section 3.3.

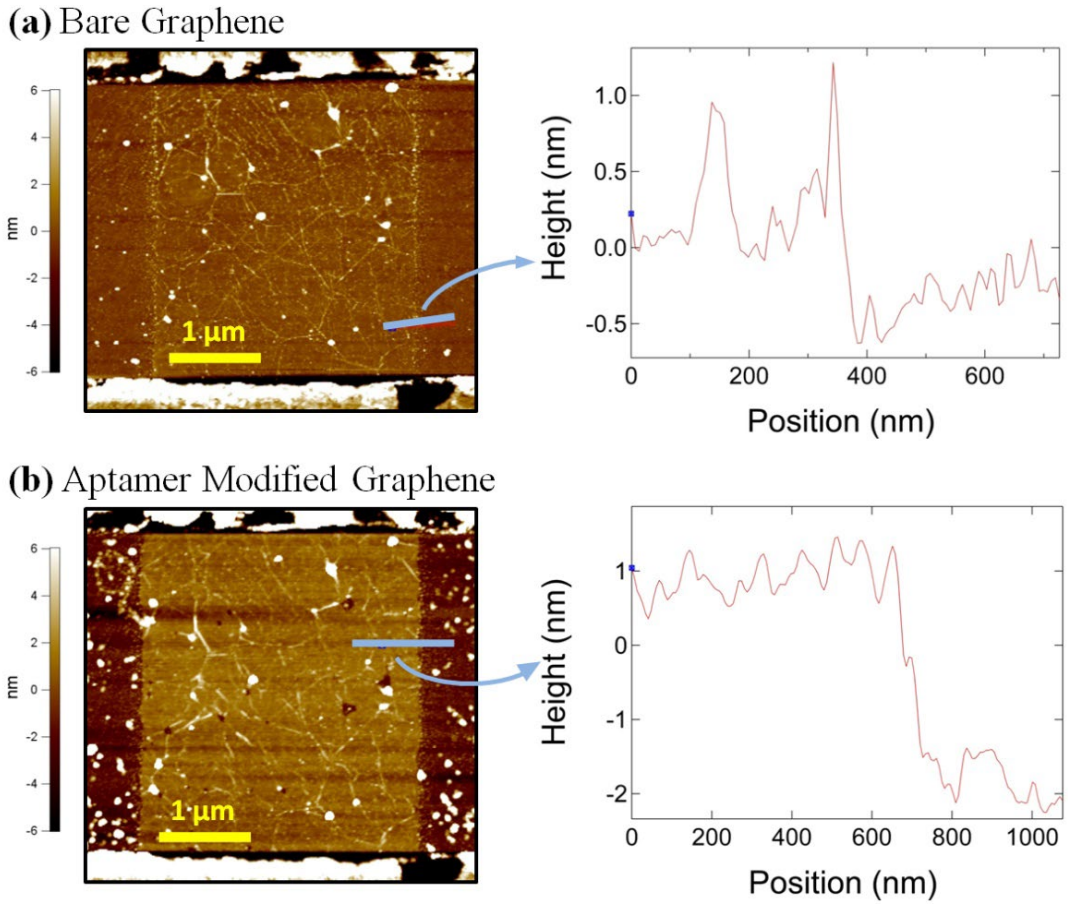


**Figure 4.6 (a)** AFM image of bare graphene channel in GFET and corresponding height profile marked by blue line. **(b)** AFM image of aptamer modified graphene channel in GFET, and corresponding height profile marked by blue line. The electrodes are located in the top and bottom ~0.5 µm portions of both AFM images. A color map of the height range is located at the left of each AFM image.

An AFM image of the bare graphene channel before functionalization shows that the height of the graphene above the substrate is ~0.5 nm. There are particles on the graphene sheet which are present in both the AFM image and height profile, however the average height of the graphene surface is ~0.5 nm. After functionalization of the PBASE and thrombin aptamer the height profile of the graphene surface increased to ~3 nm, suggesting that the thrombin aptamer was bound to the PBASE on the graphene surface. The AFM image of the aptamer modified graphene shows that some thrombin aptamer and other particles were introduced to the left and right of the

graphene channel on the bare substrate. This is most likely a result of the functionalization process contaminating the surface.

### *4.2.3 Thrombin Biosening*

A microfluidic channel was fitted to the aptamer modified GFET and the flow system was set up according to Fig 3.4. Before the biosensing experiment was performed, the device was flushed with ethanol for 20 minutes to check for leaks, clean the microfluidic channel, and remove any air that may have been in the flow system. After flushing the system, a 1mM MES buffer (pH 7.21) was added and we searched for a device with ideal sensing characteristics, i.e., a device which had a steep current ($I$) vs. liquid-gate voltage ($V_{lg}$) curve. When the protein binds to the aptamer on the graphene surface it is essentially shifting the Fermi energy and hence changing $V_{lg}$. On the steepest part of the $I$ vs. $V_{lg}$ curve, any small change in $V_{lg}$ will result in a large change in $I$ and allow us to observe a measurable change in current when the protein binds to the aptamer during the sensing experiment.

Faradaic currents were measured and were less than 1 nA. The aptamer modified device was p-doped with a charge neutrality point at approximately 200 mV prior to the sensing experiment (Fig 4.7a). The source-drain voltage was set at 25 mV. $V_{lg}$ was fixed at 50 mV and the current was observed over approximately 5 minutes to make sure there were no transient currents or excessive noise. 100 nM thrombin in a 1 mM solution of MES buffer was then added to the system. Approximately 13 minutes after the addition of thrombin there was a significant change in current (Fig 4.7b).

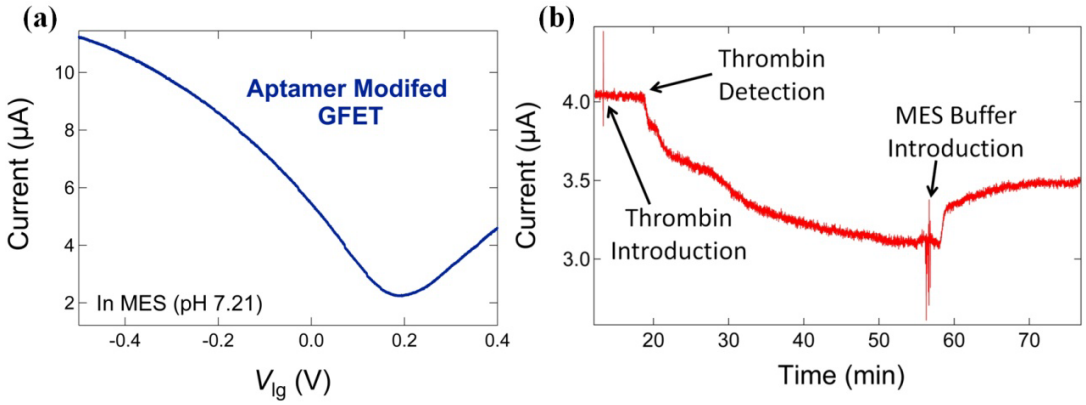


**Figure 4.7 (a)** *I* vs. $V_{lg}$ curve of the GFET device in a MES buffer. Positively charged thrombin protein causes the threshold voltage to shift in the negative direction, making the device more n-type. **(b)** Current vs. time for the aptamer modified GFET device during the thrombin biosensing experiment. The sharp spikes around the introduction of thrombin and the MES buffer are noise associated with switching of the syringes.

This change in current can be partially attributed with the positively charged thrombin protein attaching to the thrombin aptamer. The solution of thrombin protein also contained a small concentration of the protein Bovine Serum Albumin (BSA). The total change in current may therefore be attributed to BSA, thrombin and other materials in the thrombin solution binding to the substrate surface, as well as thrombin protein attaching to the thrombin aptamer. The positively charged thrombin is expected to repel positive carriers from the p-type graphene, thereby reducing the current in the channel.

Immediately after the detection event there was a sharp decrease in current which eventually tapered off after approximately 5 minutes. This sharp decrease in current can be associated with the rapid delivery of thrombin protein to the bare aptamer modified GFET device. After the binding sites began to be filled, fewer vacant sites on the aptamer modified graphene surface were available and the rate of binding slowed. At approximately 55 minutes the device was near saturation, i.e., there were no more binding sites available for the thrombin protein. A 1 nM MES buffer was then added to the system. The introduction of the MES buffer caused a sharp increase in current which can be associated with thrombin protein being removed from the aptamer

modified graphene surface. The signal stabilizes again at approximately 70 minutes, i.e., all the protein that was bound to the aptamer modified graphene surface had been removed.

In Figure 4.7b it is apparent that after the device was saturated at approximately 70 minutes the current did not increase to the initial current before the addition of the thrombin. We should expect the current to increase to its initial value after the addition of the MES buffer if the total change in resistance is attributed entirely to the thrombin protein binding to the aptamer modified graphene surface. The overall change in current from ~4 μA to ~3.5 μA may be attributed to BSA, thrombin, and other materials present in the thrombin protein solution that were tightly bound to the substrate surface near the graphene channel and were unable to be removed by the MES buffer.

CHAPTER 5

# Conclusion

## 5.1 Conclusion

The main objective of this project was to address the development of a fabrication method for CVD graphene-based FET biosensors. The successful development of these devices was demonstrated by the detection of thrombin protein. It was found that an initial device fabrication process was not suitable for biosensing applications due to heavy p-doping and surface contamination. These problems were mitigated by using a new source of CVD graphene, limiting graphene's exposure to photoresist, and an annealing process before the aptamer functionalization scheme. Future work could be performed to observe specific detection, and to determine the detection limits of the device by modulating the concentration of thrombin protein in the mass transport system. The successful detection of thrombin protein with these devices shows that CVD graphene-based FET devices may be promising candidates for the commercialization of a portable and accurate POC biosensing device.

# REFERENCES


1. A. H. Castro Neto, F. Guinea, N. M. R. Peres, K. S. Novoselov, and A. K. Geim, "The electronic properties of graphene," Rev Mod Phys **81** (1), 109–162 (2009).

2. K. S. Novoselov, D. Jiang, F. Schedin, T. J. Booth, V. V. Khotkevich, S. V. Morozov, and A. K. Geim, "Two-dimensional atomic crystals," P Natl Acad Sci USA **102** (30), 10451-10453 (2005).

3. K. S. Novoselov, A. K. Geim, S. V. Morozov, D. Jiang, Y. Zhang, S. V. Dubonos, I. V. Grigorieva, and A. A. Firsov, "Electric field effect in atomically thin carbon films," Science **306** (5696), 666–669 (2004).

4. Y. Wang, Z. Li, J. Wang, J. Li, and Y. Lin, "Graphene and graphene oxide: biofunctionalization and applications in biotechnology," Trends in biotechnology **29** (5), 205–212 (2011).

5. F. Schwierz, "Electronics: industry-compatible graphene transistors," Nature **472** (7341), 41–42 (2011).

6. Y. Wu, Y. M. Lin, A. A. Bol, K. A. Jenkins, F. Xia, D. B. Farmer, Y. Zhu, and P. Avouris, "High-frequency, scaled graphene transistors on diamond-like carbon," Nature **472** (7341), 74–78 (2011).

7. S. Watcharotone, D. A. Dikin, S. Stankovich, R. Piner, I. Jung, G. H. B. Dommett, G. Evmenenko, S. E. Wu, S. F. Chen, C. P. Liu, S. T. Nguyen, and R. S. Ruoff, "Graphene-silica composite thin films as transparent conductors," Nano Letters **7** (7), 1888–1892 (2007).

8. W. Yang, K. R. Ratinac, S. P. Ringer, P. Thordarson, J. J. Gooding, and F. Braet, "Carbon nanomaterials in biosensors: should you use nanotubes or graphene?," Angew Chem Int Ed Engl **49** (12), 2114–2138 (2010).

9. Longhua Tang Haixin Chang, Ying Wang, Jianhui Jiang, Jinghong Li, "Graphene Fluorescence Resonance Energy Transfer Aptasensor for the Thrombin Detection," Analytical Chemistry **82** (6), 2341–2346 (2010).

10. Y. Ohno, K. Maehashi, and K. Matsumoto, "Label-Free Biosensors Based on Aptamer-Modified Graphene Field-Effect Transistors," Journal of the American Chemical Society **132** (51), 18012–18013 (2010).

11. A. Sassolas, B. D. Leca-Bouvier, and L. J. Blum, "DNA biosensors and microarrays," Chemical reviews **108** (1), 109–139 (2008).

12. P. Sarkar, P. S. Pal, D. Ghosh, S. J. Setford, and I. E. Tothill, "Amperometric biosensors for detection of the prostate cancer marker (PSA)," Int J Pharm **238** (1–2), 1–9 (2002).

13. H. Y. Zhu, J. D. Suter, I. M. White, and X. D. Fan, "Aptamer based microsphere biosensor for thrombin detection," Sensors-Basel **6** (8), 785–795 (2006).

14. Ibrahim Abdulhalim, Mohammad Zourob, and Akhlesh Lakhtakia, "Surface Plasmon Resonance for Biosensing: A Mini-Review," Electromagnetics **28** (3), 214–242 (2008).

15. K. Balasubramanian and M. Burghard, "Biosensors based on carbon nanotubes," Analytical and bioanalytical chemistry **385** (3), 452–468 (2006).

16. G. J. Zhang, J. H. Chua, R. E. Chee, A. Agarwal, and S. M. Wong, "Label-free direct detection of MiRNAs with silicon nanowire biosensors," Biosensors & bioelectronics **24** (8), 2504–2508 (2009).

17. T. Kuila, S. Bose, P. Khanra, A. K. Mishra, N. H. Kim, and J. H. Lee, "Recent advances in graphene-based biosensors," Biosensors & bioelectronics **26** (12), 4637–4648 (2011).

18. S. A. Soper, K. Brown, A. Ellington, B. Frazier, G. Garcia-Manero, V. Gau, S. I. Gutman, D. F. Hayes, B. Korte, J. L. Landers, D. Larson, F. Ligler, A. Majumdar, M. Mascini, D. Nolte, Z. Rosenzweig, J. Wang, and D. Wilson, "Point-of-care biosensor systems for cancer diagnostics/prognostics," Biosensors & bioelectronics **21** (10), 1932–1942 (2006).

19. C. H. Lu, H. H. Yang, C. L. Zhu, X. Chen, and G. N. Chen, "A graphene platform for sensing biomolecules," Angew Chem Int Ed Engl **48** (26), 4785–4787 (2009).

20. I. Heller, S. Chatoor, J. Mannik, M. A. G. Zevenbergen, C. Dekker, and S. G. Lemay, "Influence of Electrolyte Composition on Liquid-Gated Carbon Nanotube and Graphene Transistors," Journal of the American Chemical Society **132** (48), 17149–17156 (2010).

21. Y. Ohno, K. Maehashi, and K. Matsumoto, "Chemical and biological sensing applications based on graphene field-effect transistors," Biosensors & bioelectronics **26** (4), 1727–1730 (2010).

22. Y. Ohno, K. Maehashi, Y. Yamashiro, and K. Matsumoto, "Electrolyte-gated graphene field-effect transistors for detecting pH and protein adsorption," Nano Lett **9** (9), 3318–3322 (2009).

23. Y. Huang, X. Dong, Y. Shi, C. M. Li, L. J. Li, and P. Chen, "Nanoelectronic biosensors based on CVD grown graphene," Nanoscale **2** (8), 1485–1488 (2010).

24. X. Dong, Y. Shi, W. Huang, P. Chen, and L. J. Li, "Electrical detection of DNA hybridization with single-base specificity using transistors based on CVD-grown graphene sheets," Adv Mater **22** (14), 1649–1653 (2010).

25. Sudip Chakraborty and C. Retna Raj, "Amperometric biosensing of glutamate using carbon nanotube based electrode," Electrochemistry Communications **9** (6), 1323–1330 (2007).

26. X. Kang, J. Wang, H. Wu, I. A. Aksay, J. Liu, and Y. Lin, "Glucose oxidase-graphene-chitosan modified electrode for direct electrochemistry and glucose sensing," Biosensors & bioelectronics **25** (4), 901–905 (2009).

27. U. Yogeswaran and S. M. Chen, "A review on the electrochemical sensors and biosensors composed of nanowires as sensing material," Sensors-Basel **8** (1), 290–313 (2008).

28. L. Tang, Y. Zhu, L. Xu, X. Yang, and C. Li, "Amperometric glutamate biosensor based on self-assembling glutamate dehydrogenase and dendrimer-encapsulated platinum nanoparticles onto carbon nanotubes," Talanta **73** (3), 438–443 (2007).

29. R. C. Becker and F. A. Spencer, "Thrombin: Structure, Biochemistry, Measurement, and Status in Clinical Medicine," J Thromb Thrombolysis **5** (3), 215–229 (1998).

30. M. L. Nierodzik and S. Karpatkin, "Thrombin induces tumor growth, metastasis, and angiogenesis: Evidence for a thrombin-regulated dormant tumor phenotype," Cancer cell **10** (5), 355–362 (2006).

31. Steven R. Garden, George J. Doellgast, Kenneth S. Killham, and Norval J. C. Strachan, "A fluorescent coagulation assay for thrombin using a fibre optic evanescent wave sensor," Biosensors and Bioelectronics **19** (7), 737–740 (2004); Radislav A. Potyrailo, Richard C. Conrad, Andrew D. Ellington, and Gary M. Hieftje, "Adapting Selected Nucleic Acid Ligands (Aptamers) to Biosensors," Analytical Chemistry **70** (16), 3419–3425 (1998); C. H. Tung, R. E. Gerszten, F. A. Jaffer, and R. Weissleder, "A novel near-infrared fluorescence sensor for detection of thrombin activation in blood," ChemBioChem **3** (2–3), 207–211 (2002).

32. Neil W. Ashcroft and N. David Mermin, *Solid State Physics*. (Saunders College Publishing, Philadelphia, PA, 1976).

33. Roald K. Wangsness, *Electromagnetic Fields*. (John Wiley & Sons, Inc., Hoboken, NJ, 1986), 2nd ed.

34. C. N. R. Rao et al., *Graphene and Its Fascinating Attributes*. (World Scientific Publishing Co. Pte. Ltd., Singapore, 2011).

35. Y. M. Lin and P. Avouris, "Strong suppression of electrical noise in bilayer graphene nanodevices," Nano Lett **8** (8), 2119–2125 (2008).

36. I. Heller, S. Chatoor, J. Mannik, M. A. Zevenbergen, J. B. Oostinga, A. F. Morpurgo, C. Dekker, and S. G. Lemay, "Charge noise in graphene transistors," Nano Lett **10** (5), 1563–1567 (2010).

37. M. S. Dresselhaus, G. Dresselhaus, and M. Hofmann, "Raman spectroscopy as a probe of graphene and carbon nanotubes," Philosophical transactions. Series A, Mathematical, physical, and engineering sciences **366** (1863), 231–236 (2008).

38. Y. Wang, D. C. Alsmeyer, and R. L. Mccreery, "Raman-Spectroscopy of Carbon Materials - Structural Basis of Observed Spectra," Chem Mater **2** (5), 557–563 (1990).

39. S. Berciaud, S. Ryu, L. E. Brus, and T. F. Heinz, "Probing the Intrinsic Properties of Exfoliated Graphene: Raman Spectroscopy of Free-Standing Monolayers," Nano Letters **9** (1), 346–352 (2009).

40. Kwanpyo Kim, Sinisa Coh, Liang Tan, William Regan, Jong Yuk, Eric Chatterjee, M. Crommie, Marvin Cohen, Steven Louie, and A. Zettl, "Raman Spectroscopy Study of Rotated Double-Layer Graphene: Misorientation-Angle Dependence of Electronic Structure," Physical Review Letters **108** (24) (2012).

41. M. A. Pimenta, G. Dresselhaus, M. S. Dresselhaus, L. G. Cancado, A. Jorio, and R. Saito, "Studying disorder in graphite-based systems by Raman spectroscopy," Physical chemistry chemical physics : PCCP **9** (11), 1276–1291 (2007).

42. Z. H. Ni, T. Yu, Y. H. Lu, Y. Y. Wang, Y. P. Feng, and Z. X. Shen, "Uniaxial strain on graphene: Raman spectroscopy study and band-gap opening," ACS nano **2** (11), 2301–2305 (2008).

43. A. C. Ferrari, J. C. Meyer, V. Scardaci, C. Casiraghi, M. Lazzeri, F. Mauri, S. Piscanec, D. Jiang, K. S. Novoselov, S. Roth, and A. K. Geim, "Raman Spectrum of Graphene and Graphene Layers," Physical Review Letters **97** (18) (2006).

44. Jun Yan, Yuanbo Zhang, Philip Kim, and Aron Pinczuk, "Electric Field Effect Tuning of Electron-Phonon Coupling in Graphene," Physical Review Letters **98** (16) (2007).

45. A. Das, S. Pisana, B. Chakraborty, S. Piscanec, S. K. Saha, U. V. Waghmare, K. S. Novoselov, H. R. Krishnamurthy, A. K. Geim, A. C. Ferrari, and A. K. Sood, "Monitoring dopants by Raman scattering in an electrochemically top-gated graphene transistor," Nature nanotechnology **3** (4), 210–215 (2008).

46. C. Stampfer, F. Molitor, D. Graf, K. Ensslin, A. Jungen, C. Hierold, and L. Wirtz, "Raman imaging of doping domains in graphene on SiO2," Applied Physics Letters **91** (24), 241907 (2007).

47. X. Dong, D. Fu, W. Fang, Y. Shi, P. Chen, and L. J. Li, "Doping single-layer graphene with aromatic molecules," Small **5** (12), 1422–1426 (2009).

48. Zhenhua Ni, Yingying Wang, Ting Yu, and Zexiang Shen, "Raman spectroscopy and imaging of graphene," Nano Research **1** (4), 273–291 (2010).

49. D. Teweldebrhan and A. A. Balandin, "Modification of graphene properties due to electron-beam irradiation," Applied Physics Letters **94** (1), 013101 (2009).

50. M. M. Lucchese, F. Stavale, E. H. Martins Ferreira, C. Vilani, M. V. O. Moutinho, Rodrigo B. Capaz, C. A. Achete, and A. Jorio, "Quantifying ion-induced defects and Raman relaxation length in graphene," Carbon **48** (5), 1592-1597 (2010).

51. L. Cançado, M. Pimenta, B. Neves, G. Medeiros-Ribeiro, Toshiaki Enoki, Yousuke Kobayashi, Kazuyuki Takai, Ken-ichi Fukui, M. Dresselhaus, R. Saito, and A. Jorio, "Anisotropy of the Raman Spectra of Nanographite Ribbons," Physical Review Letters **93** (4) (2004).

52. E. Martins Ferreira, Marcus Moutinho, F. Stavale, M. Lucchese, Rodrigo Capaz, C. Achete, and A. Jorio, "Evolution of the Raman spectra from single-, few-, and many-layer graphene with increasing disorder," Physical Review B **82** (12) (2010).

53. F. Tuinstra, "Raman Spectrum of Graphite," The Journal of Chemical Physics **53** (3), 1126 (1970).

54. L. M. Malard, M. A. Pimenta, G. Dresselhaus, and M. S. Dresselhaus, "Raman spectroscopy in graphene," Physics Reports **473** (5–6), 51–87 (2009).

55. M. S. Dresselhaus, A. Jorio, M. Hofmann, G. Dresselhaus, and R. Saito, "Perspectives on carbon nanotubes and graphene Raman spectroscopy," Nano Lett **10** (3), 751–758 (2010).

56. A. Gupta, G. Chen, P. Joshi, S. Tadigadapa, and P. C. Eklund, "Raman scattering from high-frequency phonons in supported n-graphene layer films," Nano Lett **6** (12), 2667–2673 (2006).

57. D. Graf, F. Molitor, K. Ensslin, C. Stampfer, A. Jungen, C. Hierold, and L. Wirtz, "Spatially resolved Raman spectroscopy of single- and few-layer graphene," Nano Lett **7** (2), 238–242 (2007).

58. C. Casiraghi, S. Pisana, K. S. Novoselov, A. K. Geim, and A. C. Ferrari, "Raman fingerprint of charged impurities in graphene," Applied Physics Letters **91** (23), 233108 (2007).

59. H. Wang, Y. Wu, C. Cong, J. Shang, and T. Yu, "Hysteresis of electronic transport in graphene transistors," ACS nano **4** (12), 7221–7228 (2010).

60. J. Moser, A. Verdaguer, D. Jiménez, A. Barreiro, and A. Bachtold, "The environment of graphene probed by electrostatic force microscopy," Applied Physics Letters **92** (12), 123507 (2008).

61. J. Sabio, C. Seoánez, S. Fratini, F. Guinea, A. Neto, and F. Sols, "Electrostatic interactions between graphene layers and their environment," Physical Review B **77** (19) (2008).